Membrane characterisation from the support to the skin layer: Application to silicon carbide (SiC) membranes

Mathilda Trevisan, Jérôme Vicente, Rémy Ghidossi, Adrien Vincent, Philippe Moulin

Membrane characterisation from the support to the skin layer: Application to silicon carbide (SiC) membranes

Mathilda Trevisan [a], Jérôme Vicente [b], Rémy Ghidossi [c], Adrien Vincent [d], Philippe Moulin [a,*]

[a] Aix Marseille Univ, CNRS, Centrale Marseille, Laboratoire de Mécanique Modélisation et Procédés Propres (M2P2 UMR 7340, Equipe Procédés Membranaires (EPM), Europôle de l'Arbois, BP80, Pavillon Laennec, Hall C, 13545 Aix en Provence cedex, France
[b] Institut Universitaire des Systèmes Thermiques Industriels (IUSTI-CNRS-UMR 6595), Aix-Marseille Université Technopôle de Château-Gombert, 5 rue Enrico Fermi, 13453 Marseille cedex 13, France
[c] Institut des Sciences de la Vigne et du Vin, UFR Œnologie, Axe Qualité et Identité du Vin, 210 Chemin de Leysotte, 33882 Villenave d'Ornon, France
[d] Saint-Gobain Research Provence, 550 Avenue Alphonse Jauffret, CS 20224, F84306 Cavaillon Cedex, France

ARTICLE INFO

Keywords:
Silicon carbide membranes
3D reconstruction
Characterisation
Microstructure properties
Nanotomography

ABSTRACT

SiC membranes are used in many industrial fields with high performances and good retention efficiency in the filtration of loaded liquids such as wastewater, oil or wine. Technologies allow to characterise membrane's surface but few allow the characterisation of its depth. This paper proposes the combination of results obtained by the usual techniques of porous materials and by 3D X-ray tomography characterisation. A morphological analysis of solid and porous phase is carried out on the total thickness of the membrane. Combination of results on all layers is relevant for the study of SiC membranes, showing not only the SiC surface properties but also the 3D description of the porous material (i.e. support, layer and skin). The definition of essential parameters to define the efficiency of a filtration such as hydrophobicity, porosity and tortuosity allows to justify the use and superior performance of SiC membranes for the filtration of loaded liquids.

1. Introduction

Silicon carbide (SiC) is increasingly used for membrane manufacturing because SiC membranes are more stable than polymeric membranes, they have a much longer lifetime, and the cleaning-sterilising process is better due to higher temperature resistance [1,2]. Therefore, these membranes can filter different types of loaded fluids with low pressure and minimal fouling. SiC membranes have relevant characteristics such as higher porosity ($\geq$ 40%), lower tortuosity [3], which could allow them to achieve increased permeate fluxes for filtration of loaded liquids as wine and residue sediments. Moreover, SiC is known to have a complex surface chemistry when it comes to its hydrophobic or hydrophilic behaviour. Indeed, as demonstrated by King et al. [4] in 1999, pure SiC has a hydrophobic behaviour. On the other hand, as oxygen links to the surface of the material, silicon carbide tends to behave closer to that of silica (SiO_2), which is hydrophilic. The membranes used in this work are purposely produced with as low levels of silica as possible, since this impurity leads to a reduction of the material's chemical resistance. As a consequence, they are primarily hydrophobic rather than hydrophilic and the chemical cleaning cycles may strip part of the extrinsic oxygen out again. So, one should expect the behaviour of the SiC material of the present study to oscillate between hydrophobicity and hydrophilicity throughout the different phases of the clarification processes. As a result of these characteristics, SiC has become, since 2010′s, a material of choice for the manufacture of mineral membranes used in the filtration of loaded liquids [5–8]. Indeed, these membranes are already commonly used in water purification [9] and wastewater treatment [10–12] but also for wine purification where experimentations showed production flows up to 1 log higher than other ceramic membranes used in the field and a good retention efficiency [13]. The successful development of membrane processes is limited by the understanding of the membrane fouling mechanisms and/or the modification of the porous structure. For a better understanding, the characterisation of membrane structure is of particular importance and many studies have been undertaken in this direction [14,15]. There has been a wide range of complementary techniques used for this purpose, such as: Scanning Electron Microscopy (SEM), measure of angle contact, mercury intrusion porosimetry and X-ray CT-tomography [16]. These tools permit the characterisation of membrane properties such as hydrophobicity, porosity, tortuosity and pore size and morphology

* Corresponding author.
E-mail address: philippe.moulin@univ-amu.fr (P. Moulin).

distribution. However, the major application of these techniques only concerns the characterisation of the membrane surface; it in no way concerns the different porous layers of the membranes having different characteristics. For this reason, this study proposes to go further by analysing, in addition to the usual descriptive methods for porous materials, the complete microstructure (all three layers) of SiC membranes by 3D reconstruction. This reconstruction is based on stacks of images obtained by X-ray tomography and then reconstructed using the computer tool iMorph [17]. In this study, surface properties and microstructure of the three layers of SiC membranes was determined by several descriptive techniques for porous media (SEM, measure of angle contact, mercury intrusion porosimetry and tomography by X-ray). These analyses were made on two of the different layers composing the SiC membrane in order to have an overview of the filtration process. All the following parameters could be obtained and cross-referenced between the different methods used: hydrophobicity, porosity, pore size distribution, grain size distribution, throats size and morphology, and tortuosity. Thus, a better understanding of the differences of filtration performances is expected.

2. Materials and methods

2.1. Microporous media

The analysed microporous media come from a SiC membrane Crystar® 0.6 μm (Saint-Gobain) membrane. It made up with 2 different layers deposited on a support:

- The mechanical support or substrate (average pore size ~ 25 μm)
- 1 Intermediate layer (pore size d50 1.5–4 μm). It can be used on its own as filter media or as support layers for the active filtration membrane if a thinner layer is deposited on its surface.
- The active microfiltration layer (average pore size ~ 0.6 μm)

The Saint-Gobain SiC membrane is consolidated by recrystallisation at high temperature by sublimation of the finest particle fractions, which recondense to form bridges between the larger grains. The recrystallisation temperature strongly depends to the SiC particle size, from 1600 °C for particle size near 500 nm up to > 2200 °C for particle size higher than 50 μm. The mechanical carrier is first manufactured by preparing a mixture containing SiC powders with two differents grain size by using a coarse grains d50 on thin grain d50 ratio set at 20. Coarse on thin powders weight ratio used is 3. Suitable additives for paste formation and extrusion like methylether cellulose and oil are used with a ratio additives on powder repectivly set at 10 and 2. Deionized water is used keeping a ratio water on powder in the range 0.18–0.25. The paste is then extruded in the form of a tubular structure with a certain number and geometry of channels. The part is then sintered at a temperature higher than 2000 °C under argon atmosphere during 1 h to create a homogeneous microstructure by recrystallisation.

Once the manufacture of the mechanical support is complete, SiC-based slurries with defined grain sizes are prepared and deposited by enduction on the walls of the mechanical support. The intermediate layer is prepared by using two differents grain size by using a coarse grains d50 on thin grain d50 ratio set at 4 and keeping d50 of coarse grains slightly above the pore size d50 of the membrane support to be coated. Coarse on thin powders ratio used is 1.5. The final layer is prepared by using only grain size having a particle size d50 below 5 μm. Suitable additives for slurry formation and enduction process like binder and dispersing agent are used with a ratio additives on powder are repectivly 1:10 and 2:10000. Deionized water is used keeping a ratio water on powder in the range 0.9–1.1. The final sintering step at 1600 °C under argon during 1 h creates a homogeneous microstructure of the membrane with a fine and controlled pore size distribution.

For this study, the samples from the different layers of the SiC membranes are cut into cylinders of different diameter and height for analysis by micro- and nanotomography. For the mechanical support and the intermediate layers (microtomography), the SiC membranes were cored from two membranes to obtain separate samples. For the active microfiltration layer (nanotomography), it was necessary to cut a sample using a TESCAN S9000 (Zeppelin 3D Metrology) which is a FIB (Focused Ion Beam) Xenon coupled with a SEM-FEG (Scanning Electron Microscopy-Field Emission Gun). This coupling allows a configuration where the focal points of the electrons and ions coincide, allowing imaging with the SEM during FIB machining, which allows a very high level of precision and the fabrication of nanostructures.

2.2. Pore size distribution by mercury intrusion porosimetry

Mercury intrusion porosimetry uses the property of mercury, which is non-wetting and does not spontaneously penetrate into the porosity, to obtain the pore size distribution and porosity of the analyzed material. A pore size distribution can be obtained from 4 nm up to about 350 μm. Consequently, mercury intrusion porosimetry is particularly suitable for materials with a wide pore size distribution, such as SiC membranes. For all layers of the SiC membrane, the mercury porosity measurements were carried out using an AutoPore IV 9500 V1.06 micrometer at the Saint-Gobain Research Provence laboratory. The volume of mercury entering the porous medium was measured at different pressures and a porosity versus pore size curve was defined according to the Washburn relationship:

$$Dp = \frac{-4 \times \gamma \times cos\theta}{Pc} \quad (1)$$

with Dp (m), γ (N.m^{-1}), θ, and Pc (Pa) respectively constrictions diameter, mercury surface tension, solid/liquid contact angle and pressure [18].

For ease of reading in this study, the 25 μm support, the 4 μm layer and the 600 nm filtration layer are respectively called mechanical support, intermediate layer and active microfiltration layer.

2.3. Contact angle measurement

The contact angle measurement technique aims to determine the wettability (hydrophobic/hydrophilic) of the membrane material. Surface energy is a good indicator of how easily molecules can adhere to the surface of the material. Materials with high surface energy are easier to wet than materials with low surface energy [19]. The experimental device used is a Digidrop Contact Angle Meter (GBX Scientific Instruments) in the Saint-Gobain Research Provence laboratory. A drop of water from 20 μL was placed on a SiC disc and the contact angle was measured. These tests are carried out on SiC discs, giving a good indication of the hydrophilic/hydrophobic character of the cylindrical membranes used. An image analysis system integrates the angle as a function of time and determines whether the drop penetrates the material.

2.4. SEM

SEM is an electron microscopy technique capable of producing high-resolution images of the surface of a sample using the principle of electron-matter interaction. The apparent microstructure of SiC membranes has been studied by high-resolution SEM (SEM Zeiss Geminisem 300).

2.5. Micro and nanotomography

X-ray micro or nanotomography is an imaging technique by absorption of X-rays which allows the object analysed to be reconstructed in three dimensions, rotating through 360°, from radiographic projections [20]. The rays transmitted after interaction with the material

are recorded by a detector placed after the sample. The samples are prepared upstream and positioned inside the conical beam constituted by the X-rays emitted from their emission focus towards the detector. The X-rays passing through the sample are attenuated by absorption and impregnate the detector to form an X-ray projection. These projections are recorded for a complete rotation of the specimen from 0° to 360°. The greyscale X-ray image obtained at the detector is then recorded. Based on all these projections, a Back-Projection algorithm is used to provide volume density information (3D reconstruction) where the grey levels of the reconstructed image reflect a local density. We can then access the differences in composition, as well as the presence of heterogeneities (pores, inclusions, *etc*.) within the sample. The difference between micro- and nanotomography lies in the resolution related to the focal spot size of the electron beam. Depending on the device, laboratory microtomographs can achieve a voxel size ranging from 0.25 to 400 μm, making it suitable for the first two layers of the SiC membrane. The nanotomograph with a resolution of 50 nm enables the structure of the active microfiltration layer to be analysed. For the characterisation of the mechanical support and the intermediate layer of the SiC membranes, microtomography was carried out at the IMI (Institut Mécanique et Ingénieurie, Aix Marseille University) with an EasyTomXL150 "Mechanic Ultra" microtomograph (RX-Solution France). The characterisation of the active layer of the SiC membrane was carried out in the CEREGE laboratory (Aix-Marseille University), by nanotomography with the UltraXRM-L200 apparatus (Zeiss, U.S.A.) equipped with a rotating anode X-ray source (Cu, Kα, 8048 keV, 40 kV acceleration voltage, 30 mA current).

3. Results and Discussion

The SiC membrane is a porous medium, therefore composed of two phases: porous and solid, each with a different absorption coefficient for incident X-rays. The result is a distinct grey level in the images: the solid phase has a lighter grey level than the darker porous phase. The 3D reconstruction is therefore carried out by separating the different phases of the structure by binarization of the image stack according to the grey levels composing the image and highlights the numbers of voxels (3D) (pixel for the 2D) belonging to the poral phase (black) and the solid phase (white). the binarization or phase segmentation is obtained by selecting a threshold to separate voxels according their grey values. This threshold is determined from the analysis of the histogram of grey levels composing the image (Fig. 1).

Fig. 1, Figs. 2 and 3 were systematically filtered with a "Non local mean" (nlmean) filter [21]. Fig. 1.1, Fig. 2.1 and Fig. 3.1 show the grey level distribution of the original images and the distribution of the filtered images. With the filter, a systematic enhancement of the images is obtained which allows an easier binarisation (phase separation). For all these samples, the classes are roughly balanced (as many voxels in the pore phases as in the solid phases). The first case (Fig. 1.1) is the most classical with two Gaussian curves having a large overlap area. In this case, the filter allowed a better separation of the two Gaussian curves. A similar behaviour can be observed in the second case (Fig. 2.1) even though in the original images the Gaussian curves were already well separated with a large intermediate area between the two peaks. In the case of Fig. 2.1, the filter further deepens the overlap area and refines the two Gaussians a bit. The third case (Fig. 3.1) is the most difficult case where the two Gaussians are completely merged.

Fig. 1.2, Fig. 2.2 and Fig. 3.2 show the cumulative grey level distributions of the filtered images. The display of the cumulative grey levels (%) allows us to know, for a given grey level value, the percentage of voxels with a grey level lower than the chosen value. The binarisation consists in finding the grey level value or threshold which separates the two phases of the medium. When the Gaussians are well separated, the ideal threshold is the one that best separates the Gaussians (125 and 75 for the active microfiltration layer and the mechanical support). The choice of the threshold is more delicate in the case of the intermediate layer. For this layer, the porosity should be close to 40% (thus balanced phases). However, only one Gaussian is observed. This can be explained by the fact that the pores are smaller and that a large part of the voxels concern voxels at the interface between the pore and the solid, leading to a drift of the values towards the intermediate grey levels. This is explained by a resolution (voxel size) that is too low compared to the size of the pore cells. In this case, the pores are small (6 μm) compared to the voxel size (2 μm), therefore the number of voxels at the interface between the pore phase and the solid phase is of the same order of magnitude as the number of voxels in the pore phase. Also, the large number of voxels at the interface (i.e. including both void and solid) fills the space between the Gaussian. This, does not allow for a good separation. In this case, the threshold is chosen here to obtain the known porosity value (40%) obtain by mercury intrusion porosimetry. The slope of the cumulative distribution indicates the sensitivity of the porosity estimate to the choice of threshold. Figs. 1.2, 2.2 and 3.2 show in grey an uncertainty zone of 10 values around the selected thresholds. Thus, we obtain a porosity of 46.5% ± 2.4%, 43.8% ± 1.6% and 40.8% ± 6% respectively for the active microfiltration layer, the intermediate layer and the mechanical support. The low resolution explains the high sensitivity for estimating the porosity in the latter case. In this last case, the pores are too small for microtomography but too large for

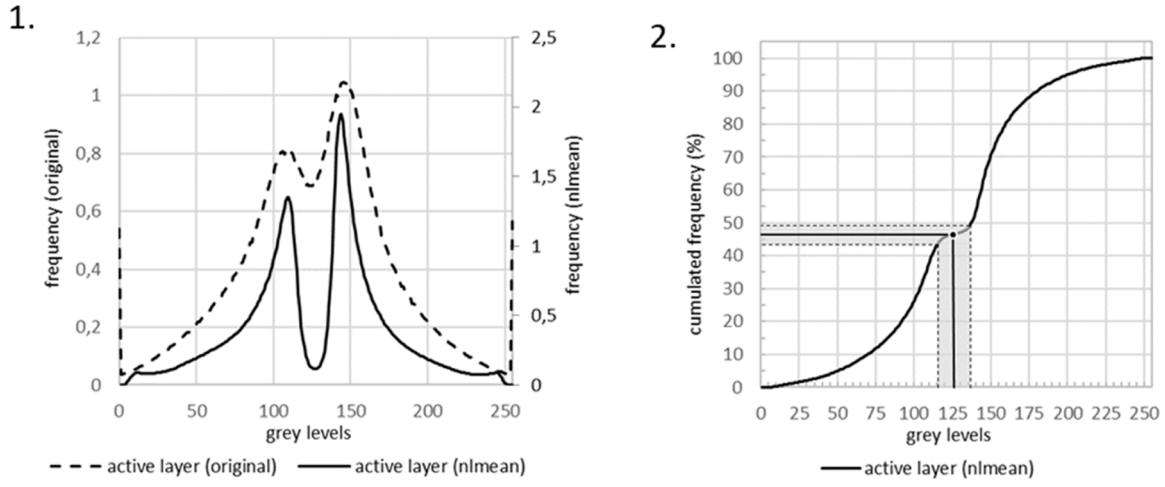

Fig. 1. Variation of (1) the grey level distribution of the original images and (2) the cumulative grey level distributions of the filtered images (active microfiltration layer).

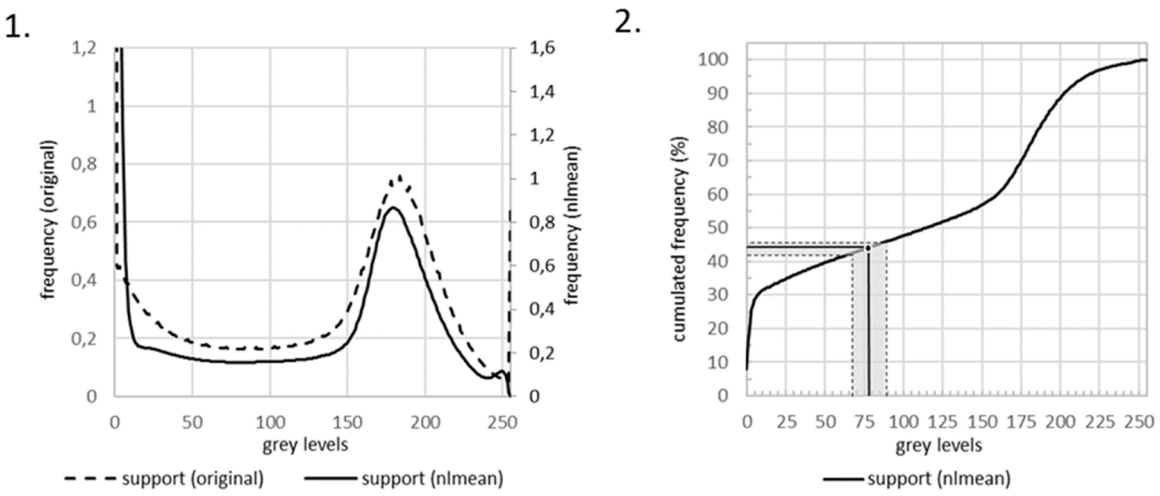

Fig. 2. Variation of (1) the grey level distribution of the original images and (2) the cumulative grey level distributions of the filtered images (Support).

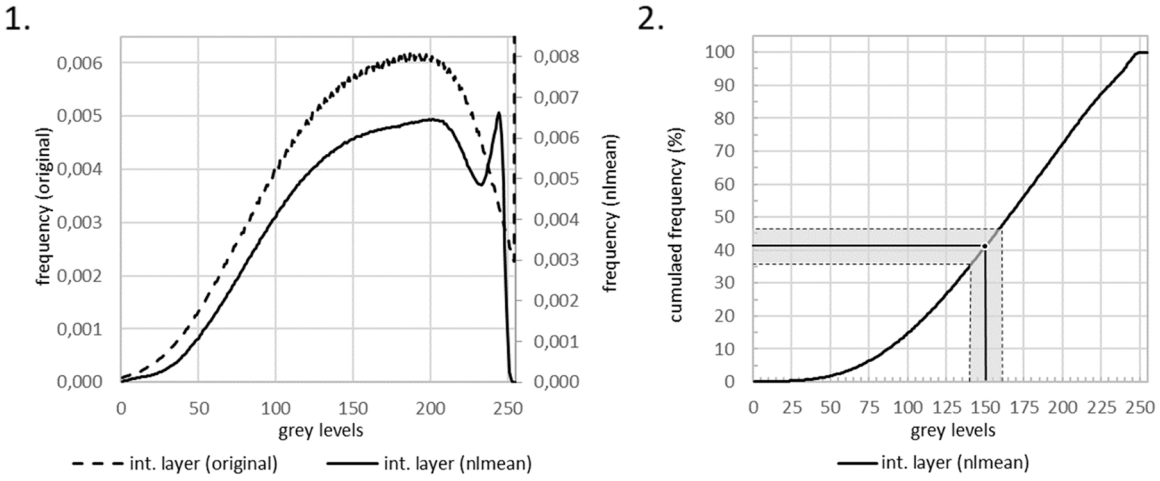

Fig. 3. Variation of (1) the grey level distribution of the original images and (2) the cumulative grey level distributions of the filtered images (Intermediate layer).

nanotomography.

In a two-phase medium (poral and solid), the classes to which these different voxels belong result in two Gaussian lines whose peaks correspond to the average intensity of the phases. The threshold, calculated from the grey level distribution of all the stack, is chosen by the Li method [22] and then applied to all slices. This threshold could also be selected in order to obtain the same porosity as the experimental one. Thus, based on this phase segmentation, all the above-mentioned morphological parameters can be calculated using algorithms and calculations defined and developed by the iMorph software. These parameters are calculated on a ROI (for Region Of Interest) (Fig. 4) defined by the user as being the most representative of the sample. In this study, the direction of fluid flow through the porous medium is always represented by the *z* axis, the horizontal slices corresponding to the axis x, y.

3.1. *Pore size distribution by mercury intrusion porosimetry*

The Crystar® 0.6 μm membrane consists of several layers with very different pore sizes (Fig. 5): a mechanical support at 25 μm, the intermediate layer (not very visible) at 1.5 μm and the active microfiltration layer at 600 nm.

Fig. 5 shows (i) the average pore diameters of the different layers analysed and (ii) their respective porosity, which is ≥ 40% for all layers. It is difficult to isolate the intermediate layer at 1.5 μm because (i) it is very thin and (ii) it is overlapping the active microfiltration layer at 600 nm.

Also for this analysis an intermediate layer of 4 μm (using as the skin for another membrane) will be studied in order to see the potential of the measurement techniques used with respect to this size. Fig. 6 shows the pore size distribution of the 4 μm filtration material.

This makes it possible to study three layers with a log difference in terms of pore size and thus obtain a good overview of the Crystar® 0.6 μm membrane.

3.2. *Hydrophobicity of SiC*

By integrating the evolution of the contact angle and volume over time, the hydrophobic/hydrophilic nature of the SiC material can be determined and the results obtained show that SiC has a higher hydrophobicity ($\Theta_{water} = 85.5°$) than the materials of some existing ceramic or organic membranes [23,24], Table 1 e.g. 1.1, 1.3 and 5.4 times more hydrophobic respectively for PVDF, alumina and the ceramic membranes TiO_2 (surface), Al_2O_3, TiO_2, ZrO_2 (support).

3.3. *SEM measurement*

Fig. 7.1 shows all three layers of the Crystar® 0.6 μm membrane from right to left: from the support (25 μm) to the active microfiltration

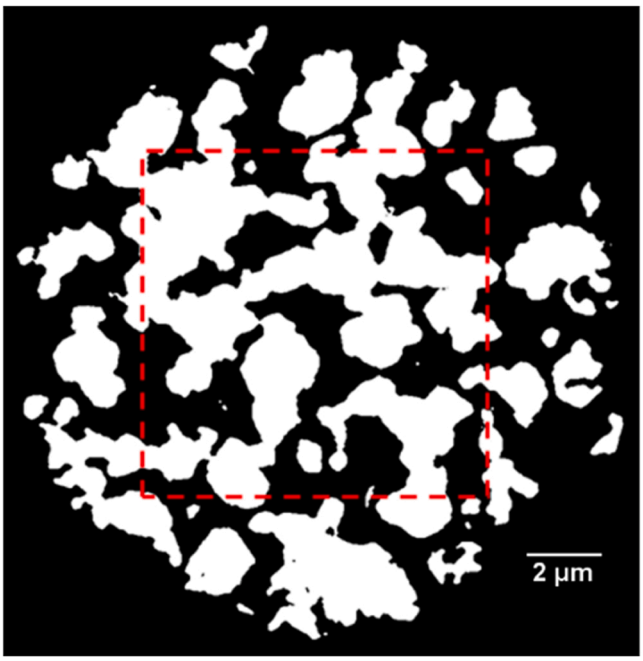

Fig. 4. Example of binarization for one image (Active layer) by nano-tomography and selection of ROI (red square).

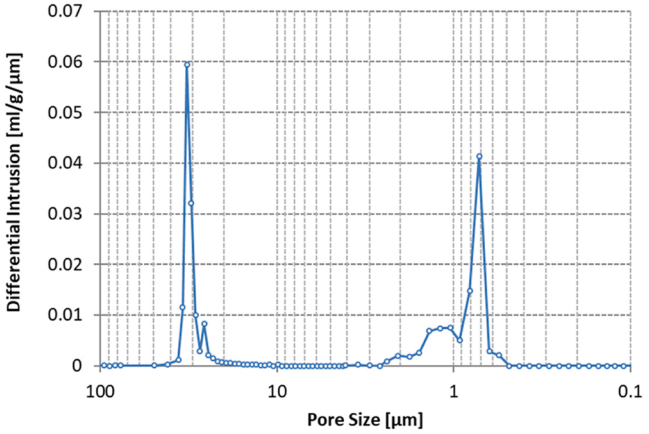

Fig. 5. Differential mercury intrusion as a function of pore size for Crystar® SiC membrane 0.6 µm.

layer (600 nm). A magnification in Fig. 7.2 shows the intermediate layer at 1.5 µm and the active microfiltration layer at 600 nm as well as their junction. Fig. 7.3 shows the consolidation of the SiC grains at high temperature. Finally Fig. 7.4 shows the grain size for the active microfiltration layer, where the grain size is approximately 400–800 nm. Fig. 7.5 represents the SEM pictures of the Crystar® SiC membrane with pore size d50 at 4 µm (Fig. 7).

3.4. Tomography

This section presents the morphological results obtained on the layers analysed with the micro tomography (the mechanical support and the intermediate layer) and nano tomography (the active microfiltration layer). Same algorithms have been applied to micro and nano tomography images.

3.4.1. Porosity estimation and variations toward filtration direction

The selection of the threshold value, therefore, allows to differentiate

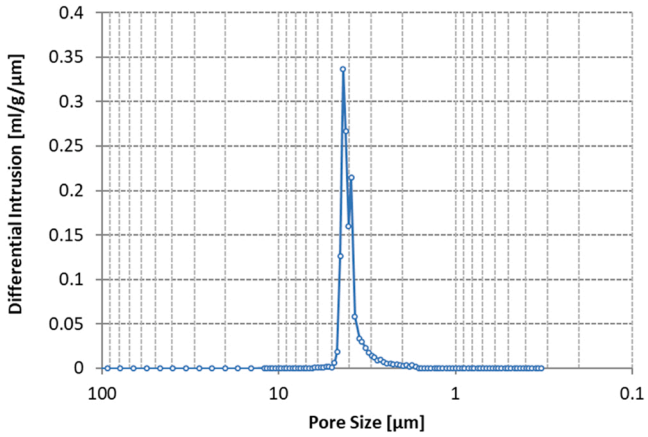

Fig. 6. Differential mercury intrusion as a function of pore size for Crystar® SiC membrane 4 µm.

Table 1
Measurement of the contact angle with water for several materials constituting ceramic membranes. With Al_2O_3 = alumina; ZrO_2 = zirconium oxide; TiO_2 = titanium oxide; PVDF = polyvinylidene fluoride and PC = polycarbonate.

Material	Water angle contact Θ_{water} (°)
SiC	**85.5**
Al_2O_3	72.4
ZrO_2	71.8
PVDF	69.3
Y_2O_3	68.3
PC	53.5
TiO_2 (surface), Al_2O_3, TiO_2, ZrO_2 (support)	15.6

between the two phases (porous and solid) and naturally allows to estimate the porosity of the samples.

The automatic threshold selection gives a mean porosity of 45% for the mechanical support, 40% for the intermediate layer (Fig. 8.1) and 47% (Fig. 8.2) for the active layer. These values are confirmed with those obtain with mercury intrusion porosimetry (Table 3) (Fig. 8).

For each sample, the porosity variations along the filtration direction (z-axis) shows a homogeneity of porosity along the ROI with fluctuations that may be related to grain size and arrangement through layers. This analysis has highlighted the difference in resolution between the samples and justifies the choice of different techniques for all the layers of the membrane. Figs. 1.2, 2.2 and 3.2 can be used to quantify the sensibility of the binarization step to the threshold value. This sensibility is depending on the grey level contrast of the images (depends on the X-ray absorption contrast inside the porous media and the x-ray acquisition parameters), but also on the partial volume effect which is related to the voxel size (Table 2) compared with the sizes of the structures (pores or grain) observed (0.6 µm/4 µm/25 µm) and to the specific surface value.

Fig. 8.2, at the threshold value chosen between the two Gaussian (119), the porosity of the active microfiltration layer is 41%. Table 3 summarise the mean porosity obtained by mercury intrusion. These results show a porosity in correlation with the other two layers of the SiC membrane and in correlation with those obtained by mercury intrusion porosimetry (Table 3).

3.4.2. Granulometry of the poral phasis and throats size morphology

To estimate a pore size distribution, morphological operations on binary images such as granulometric opening can be used to directly retrieve the pore size distribution (PSD). Another method to access the PSD is to determine the map of aperture diameters. The local aperture diameter [25] is defined for any point P of an object as the diameter of the largest ball totally included in the object and containing the point P. The volume distribution (number of voxels) of these aperture values

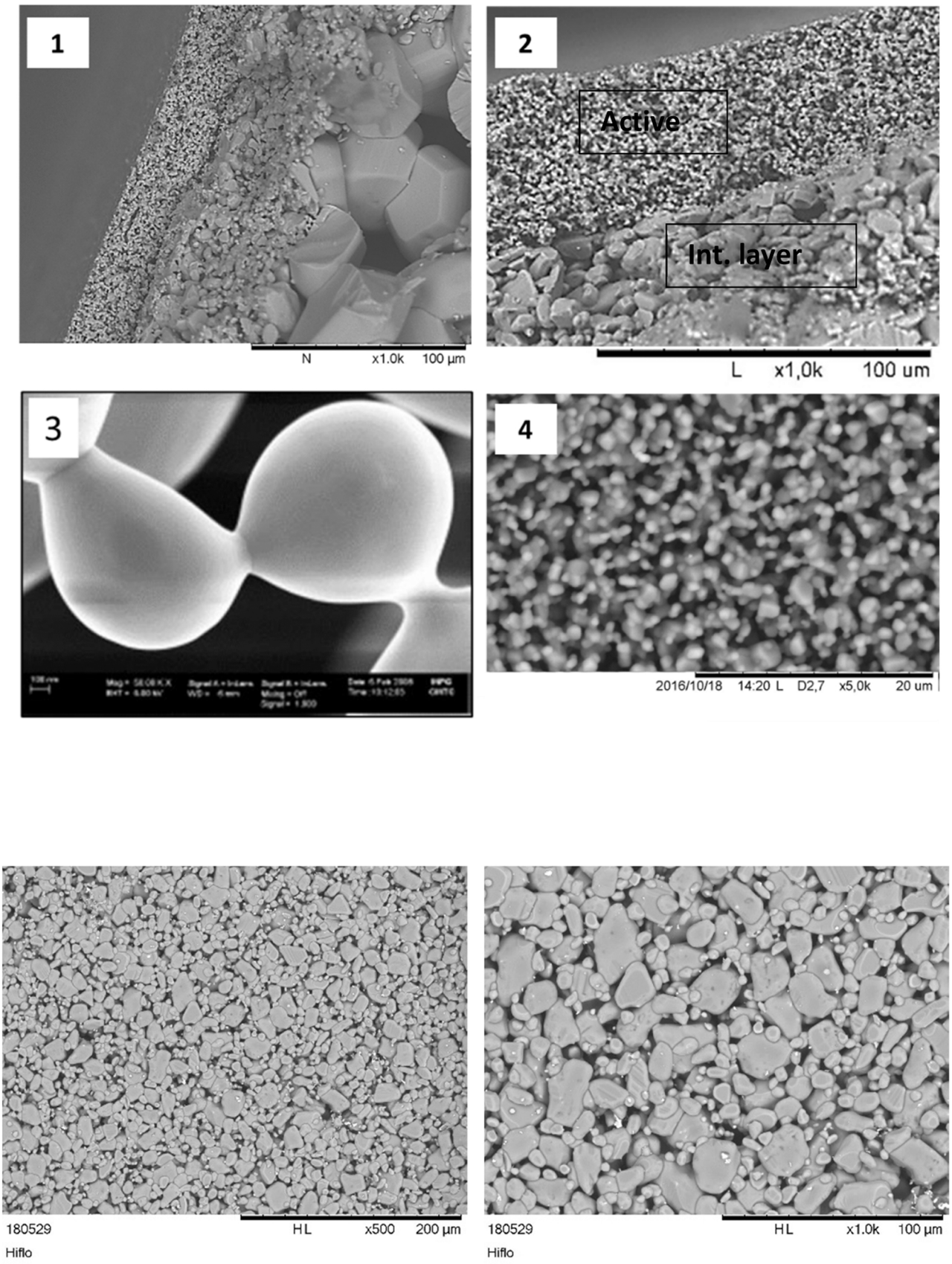

Fig. 7. SEM characterisation of (1) the 3 layers of the Crystar® 0.6 µm membranes, (2) the intermediate layer (1.5 µm) and the active microfiltration layer (600 nm), (3) SEM magnification of the consolidated SiC grains at high temperature, and (4) SEM characterisation of the active microfiltration layer (600 nm) for which the grain sizes are approximately 400–800 nm.(5) SEM picture of Crystar® SiC membrane 4 µm.

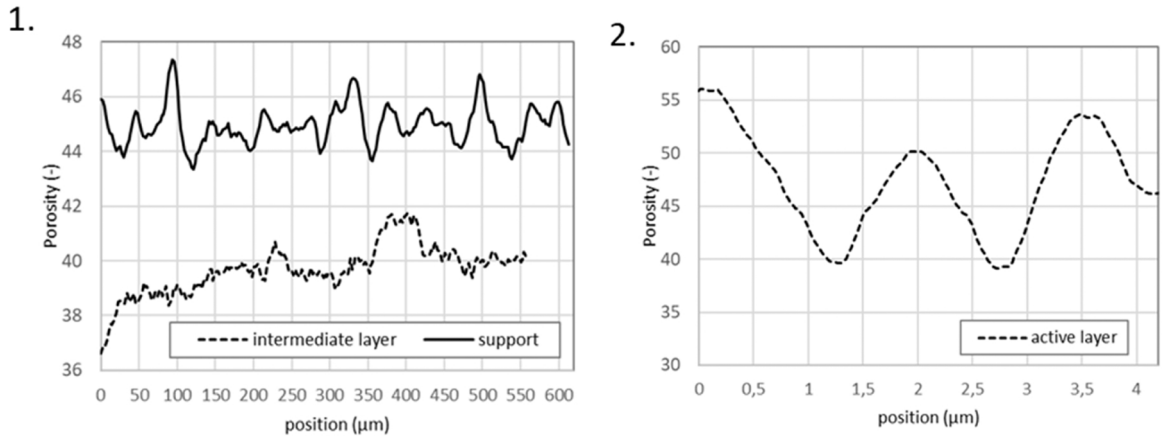

Fig. 8. Distribution of the porosity as a function of the position along the length of the filtration for (left) the mechanical support and intermediate layer and (right) the active layer.

Table 2
Sample characteristics and ROI for all membrane layers (L = with; l = length and h = height of the sample).

Sample	Cylindrical sample (øxh µmxµm)	Voxel size (µm)	Initial volume to be processed (Lxlxh; voxels)	ROI dimensions (Lxlxh; voxels)
Mechanical support	1000 × 1000	2.28	964 × 902 × 948	500 × 500 × 500
Intermediate layer	1000 × 500	2.07	1099 × 1119 × 1121	450 × 450 × 270
Active layer	77.5 × 16	0.0163	894 × 874 × 908	540 × 540 × 330

Table 3
Summary of the characteristics obtained by mercury intrusion porosimetry on the different layers of the SiC membrane. The values for the mechanical support and the "intermediate layer" from the front microfiltration membrane are given as an order of magnitude. The layers shown in red are the different layers analysed in this study.

	Mechanical support	Intermediate layer	Active layer (Crystar® 0.6 µm)
Thickness (µm)	≥ 1 mm	≤ 1 mm	40 µm
Average pore diam.	24.5 µm	4 µm	0.6 µm
Porosity (%)	45	39	51

gives an overview of the most representative diameter value and makes it possible to determine the pore diameter of the porous medium in a first estimation [15]. Fig. 9 shows the aperture values distribution of the poral phase of the 3 different layers.

For each maximum ball size class, the number of voxels concerned is plotted on ordinates. It should be noted that this measurement is not representative of local constrictions of the pore topology as maximal included ball are principally located at pore centres and more rarely at constriction centres. For the mechanical support the average pore size is 26.5 µm, 5–6 µm for the intermediate layer and 662 µm for the active microfiltration layer. (Fig. 9). These values are close but systematically slightly higher to the pore sizes obtained by mercury intrusion (Table 3). It is noteworthy that the pore size estimation by mercury intrusion is also sensible to the passage diameters between pores (throats or constrictions). Fig. 10.

The throats that are the passage windows between pores correspond to the topological constrictions where the particles suspended in the solution to be filtered will have to pass through the membrane. Therefore it is interesting to know their size and morphology. From an automatic pore segmentation using maximal balls identification and watershed labelisation [26], voxels located at the passage window between two neighbour pores constitutes a surface called constriction or throats (see part 3.4.3 for additional details on cells and throats identifications) Fig. 11.

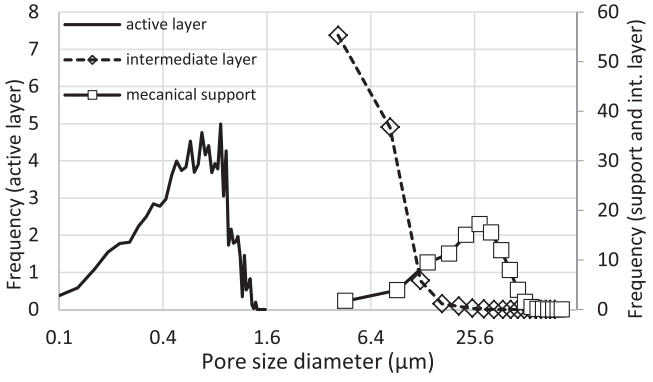

Fig. 9. Aperture values distribution of the poral phase of the 3 different layers: intermediate layer, mechanical support; mean diameter 670 nm, 6 µm, 26 µm respectively.

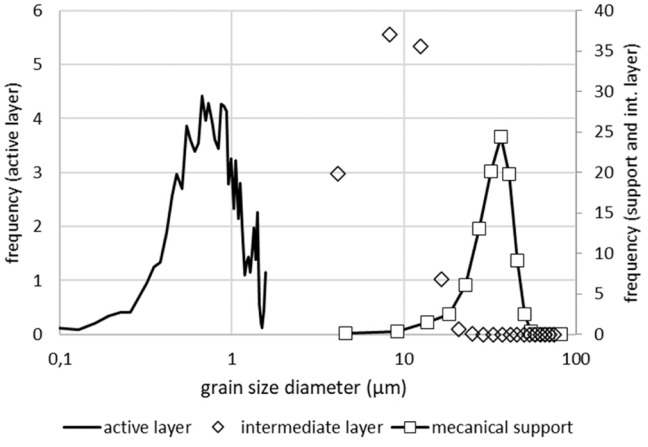

Fig. 10. Grain size distribution as a function of grain size. [Solid phase of the active microfiltration layer (600 nm)].

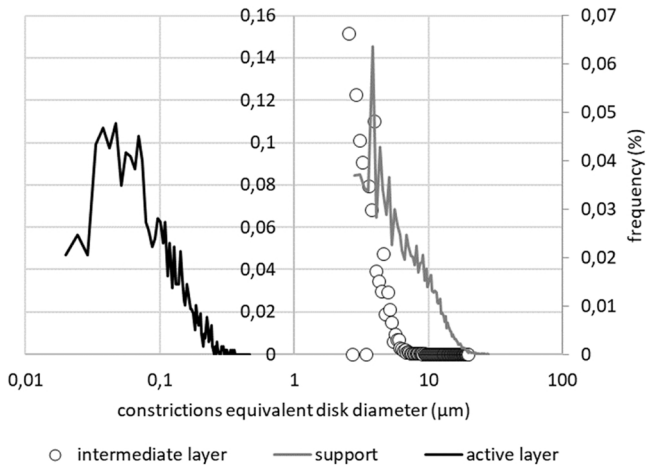

Fig. 11. Distribution of constriction diameter (diameter of same surface disk) for active layer, intermediate layer and mechanical support; mean diameter 662 nm, 5.9 µm, 26.4 µm respectively.

The shape analysis of this surface is obtained from the analysis of the inertia matrix of the voxels composing each constriction. eigenvalues and eigen vectors of the inertia matrix give the dimensions and orientations (major and minor axis of the throat equivalent ellipsoid). The diameter of the disc with the same surface area is also calculated. Pore and grain size as well as morphological characteristics of throats are presented in Table 4.

3.4.3. Calculated Molecular Weight Cut-Off (MWCO), penetration depth and accessible volume

The cut-off size determination method from 3D images presented in this paper uses a decomposition of the pore space into interconnected cells linked together by constrictions. This technique using a pore network approach is a faster variant of the method published in the article by Nathan et al. [16] and which also makes it possible to define different passage diameters from the morphological data of the constrictions and cells. The cells are obtained from the calculation of the aperture map used previously and which allows to identify the set of the maximum spheres within the pore space. The centres of these spheres are then used as foci of cells whose final shape is obtained by a watershed markers-based method [27]. This segmentation ensures that all cells contains a single maximum sphere and are necessary surrounded by constrictions (throats) that connect other cells.

Voxels that belong to constrictions can be easily obtained by scanning the labelised watershed map. The gravity centre of constrictions voxels, and of cells voxels constitutes the constrictions nodes and cells nodes of the pore network respectively. To complete this network, we identify the pores in contact with the entry and exit faces of the simulation. The centres of these faces constitute the edge nodes of the porous network thus obtained. The morphological data of the cells, of the flat objects such as constrictions or faces are assigned to their corresponding network nodes. For the simulation we choose as local diameter the inscribed spheres diameter for cell nodes and the inscribed disc diameters for constrictions or faces nodes. The injection face nodes constitute the entry points for the simulation. The largest inlet diameter is identified first. All face nodes with a diameter greater than or equal to this largest diameter are invaded, and the nodes connected to them are pushed into the list of potentially invaded nodes. If their diameters are also greater than or equal to the current maximum diameter then they are considered as invaded nodes. We remove them from the list of potentials invaded and the non-invaded nodes connected to them are added to the list. For the current maximum diameter, the iterative process stops when no more points in the list have diameter greater than or equal to the current maximum diameter. the current maximum diameter (that correspond to the maximum particle size that can reach this node) is assigned to the nodes that have been invaded at the previous step. The next step consists of repeating this invasion procedure using a smaller maximum diameter. The next diameter can be chosen by searching for the next maximum diameter from the non-invaded nodes of the entry face and from the list of potential invaded nodes, or in other words from the border of the propagation front. We can also fix the total number of iterations to finish the invasion algorithm. Once the number of iterations is fixed, we deduce the size increment to be subtracted from the current maximum diameter to constitute the new maximum diameter.

When all the nodes have been reached then the simulation stops, and we affect to the voxels of the different segmented objects (cells, faces, constrictions) the values of the largest particle diameters that could reach their items. Fig. 12 illustrates for the sake of clarity the method by representing the pore network of a flat porous medium. Red nodes are the cells centres, green nodes are the face or constrictions centres. In Fig. 12 constrictions are represented by voxels walls and we can verify that they are located at topological constrictions of the poral space. The grey levels of the section plane at the bottom of the image correspond to particle diameter capable of reaching the various cells in the medium (white for big particles diameter and black for small ones).

We can calculate the accessible volume for each particle diameter by summing the voxels which have for value an accessible diameter greater than or equal to the considered particle size. Note that these volumes are, by constructions of the propagation method, the volumes accessible from the injection face only. Also, the maximum attainable depth or penetration length for a particle size can be deduced from the accessible volume map, by calculating the maximum depth (distance to the entry face) of voxels with accessible volume greater than or equal to the considered particle size. The accessible map colour refers to the biggest particle able to reach this cell. (Fig. 12).

The analysis of the indexed map gives can be used to estimate a pure geometrical cut-off as we can identify maximal radius that connect injection and exit face, moreover we can also identify for this diameter the volume of pores that is accessible for a particle of same diameter. The MWCO are defined for all the studied membranes (Fig. 13) and seems in agreement with the values obtained by mercury intrusion porosimetry. Fig. 13 shows that for the active filtration layer the largest particle that can pass through the entire ROI measures 707 nm but has access to only 14% of the pore volume. The cut-off value can be arbitrary chosen when the curve of the maximal depth drops sharply and when at the same time the accessible volume goes below 50% of the total sample depth. The MWCO thus determined are consistent with mercury intrusion porosimetry but slightly above (The throats that are the passage windows between pores correspond to the topological constrictions where the particles suspended in the solution to be filtered will have to pass through the membrane. Therefore it is interesting to know their size and morphology. From an automatic pore segmentation using maximal balls

Table 4
Summary of the dimensions of the constrictions for the set of ROI of each analysed samples. With s = standard deviation.

		Mechanical support	Intermediate layer	Active layer
		mean (µm) ± s	*mean* (µm) ± s	*mean* (nm) ± s
Pores	Aperture diam.	*26.4* ± 10	*5.86* ± 2.9	662 ± 267
Grains	Aperture diam.	33.7 ± 7.6	8.83 ± 3.3	827.3 ± 305.5
Constrictions				
Equivalent disk diam.		16.9 ± 11.5	5.6 ± 2.6	370 ± 265
Major axis diam.		21.6 ± 15.3	6.7 ± 4.1	470 ± 347
Minor axis diam.		12.9 ± 9.5	3.6 ± 2.8	287.8 ± 214.4

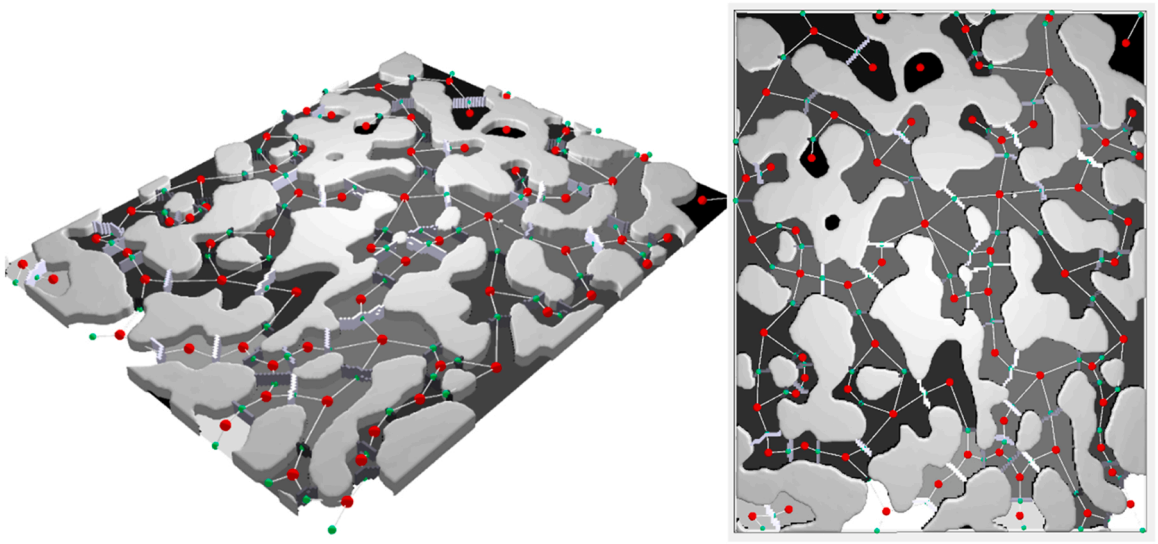

Fig. 12. Method used for MWCO determination. Visualisation of the pore to throats network (red nodes are pores centres, green sphere are throat nodes and faces input or output) throats nodes are localised at throats voxels barycenters. The colour of the throat voxel (from black to white) represent the local dimension of the throat (inner disk diameter). The grey level slice at the bottom of the view represent the accessible map where the grey level is related to the particle size able to reach a pore by going through its surrounded throats. White zone corresponds to largest particles and black zones to smallest ones.

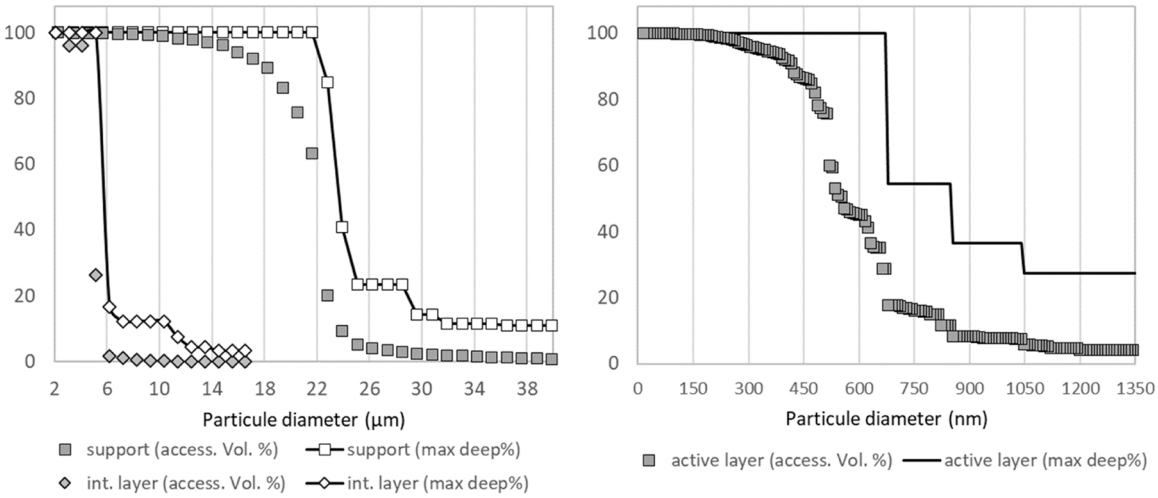

Fig. 13. A dimensioned penetration depth and accessible volume as a function of particle diameter for (left) mechanical support and intermediate layer and (right) active microfiltration layer.

identification and watershed labelisation [26], voxels located at the passage window between two neighbour pores constitutes a surface called constriction or throats (see part 3.4.3 for additional details on cells and throats identifications). The shape analysis of this surface is obtained from the analysis of the inertia matrix of the voxels composing each constriction. eigenvalues and eigen vectors of the inertia matrix give the dimensions and orientations (major and minor axis of the throat equivalent ellipsoid). The diameter of the disc with the same surface area is also calculated. Pore and grain size as well as morphological characteristics of throats are presented in Table 4). We can remark that the MWCO gives a particle size bigger than the mean constrictions diameter showing that it is important to take the real topology of the pore network to estimate membrane property. Moreover numerical MWCO gives also the total volume that is theoretically (geometrically) accessible for every particle size and in comparison with other technics, there is no dependence on solute or solvent. We can also observe in Fig. 13 (for support and active layer) that for particle size close to the mean constriction diameter, the accessible volume start to decrease while particle can cross the total sample.

However, precautions must be taken regarding representativeness of ROI's used for the 3D images analyzes. The used Roi's side correspond to approximatively to 15, 160 and 44 for active layer, the intermediate layer and the respectively. the representativity for the support is good and the resolution is also adapted. For the intermediate layer the representativity is good but the resolution is low. For the active layer, representativity is low but the resolution is good. The ROI size limitation of the active layer is principally due to the FIB preparation. Indeed, the 3D reconstruction of the ROI studied for the microfiltration active layer shows impacts on the edges of the ROI potentially due to the FIB treatment which could bias the MWCO results (Fig. 14). we can also notice for this layer that the usable depth is weak to perform MWCO computation as only few throats may be cross toward the filtration direction.

3.4.4. Tortuosity

Tortuosity is related to the minimal geometric path in a media to go

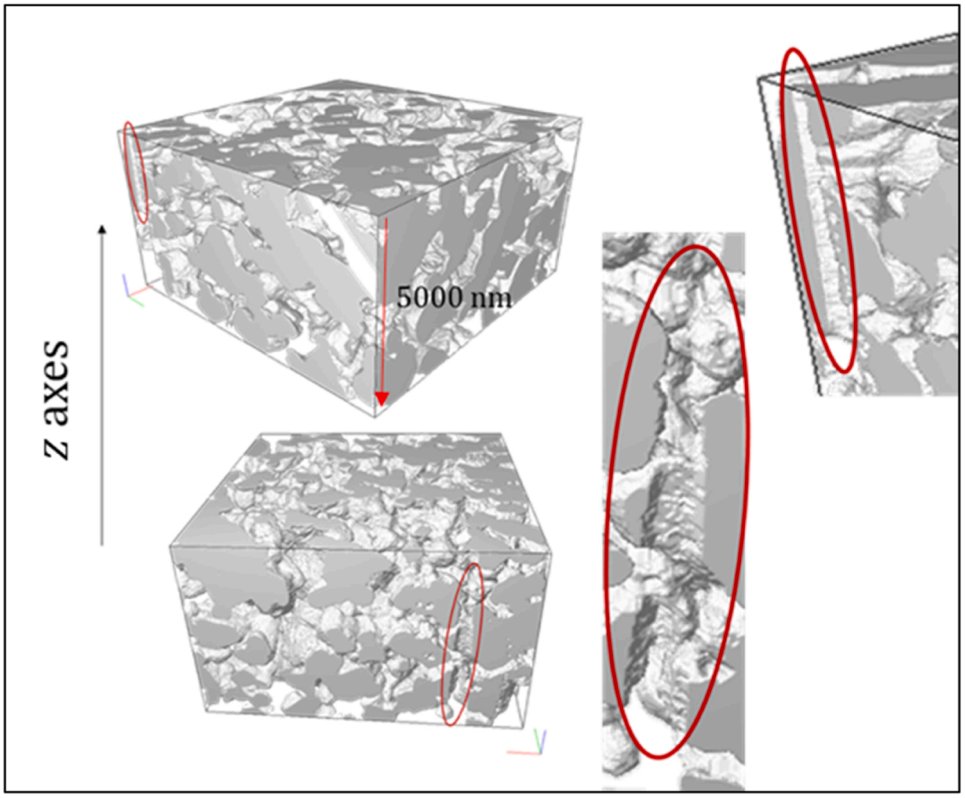

Fig. 14. 3D reconstruction of the ROI of the microfiltration active layer (600 nm) showing laser impact due to FIB treatment.

from one point to another and requires the calculation of the geodetic distances necessary to define the minimal path. The Dijkstra algorithm is a graph search algorithm that solves the problem of the shortest path [28]. Tortuosities are calculated in this present work from the networks or graphs connecting adjacent cells via the centres of their respective passes. The pore-constriction-pore graph thus imposes on the minimal path to pass through the centre of the pores and the centre of the constriction. Thus the shortest paths are calculated on all the arrival points of the graph from the opposite face (x_{max}, y_{max} or z_{max}) to the starting or injection face (x_{min}, y_{min} or z_{min}) and the tortuosity can be defined. This characteristic is studied on the three axes because it provides information on the anisotropy of the medium: if the tortuosity value depends on the direction (differs along one axis) then the medium is considered anisotropic, otherwise it is considered isotropic.

Table 5. shows the average tortuosity values of the different layers according to x, y and z. Regardless of the axis, the tortuosity of the ROI is approximately between 1.1 and 1.3. These low tortuosity values may justify the significantly higher permeabilities of SiC membranes compared to more tortuous ceramic oxides membranes with a tortuosity around 3 given by the manufacturer.

4. Conclusion

The analysis of the properties of SiC and the microstructure of the membranes has made it possible to use various descriptive and complementary technologies for porous media, including nanotomography. The possibility to reconstruct in 3D using the iMorph software allows a better understanding of the structure of SiC membranes with additional information. The measurement of the contact angle of the membranes made it possible to determine the greater hydrophobicity of SiC (Θ_{water} = 85.5°). The three layers of the membrane analysed by micro- and nanotomography and then reconstructed in 3D enabled numerous structural properties to be extracted: average pore diameter, morphology of the constructions which are essential information for understanding the passage of particles within the pores during filtration. In addition, a homogeneity of the structural properties between the three layers was observed. The porosity and pore sizes measured with mercury intrusion porosimetry proved to be in agreement with the values obtained in tomography. However, for the active microfiltration skin layer, the sample preparation performed by FIB damaged the sample by digging grooves in its depth. Thus, the region analysed by nanotomography was slightly damaged and the representativeness of the sample was thus reduced. For the first time an accessible map colour refers to the biggest particle able to reach this cell is produced for each layer to estimated MWCO. The calculated particle accessible volume also provides new and relevant information for the use of SiC membranes: what proportion of the pore space is accessible for a given particle size. The calculation of the tortuosity over the whole membrane shows a very low tortuosity of the SiC membranes (~ 1.2) compared to other oxide ceramic membranes.

Table 5
Summary of tortuosity averages based on minimal path computed on throat network graph. Each principal directions are computed for the ROI of each of the samples of the three membrane layers.

	Mechanical support	Intermediate layer	Active layer
Tortuosity	mean±s	mean±s	mean±s
x	1.2 ± 0.01	1.2 ± 0.01	1.3 ± 0.1
y	1.1 ± 0.01	1.1 ± 0.01	1.2 ± 0.09
z	1.2 ± 0.02	1.3 ± 0.04	1.2 ± 0.07

Funding

Not applicable.

Authors contributions

MT: experiments and writing the first paper, RG: experiments and

supervision, JV: modelisation and corrected the paper, PM supervision and writing the paper.

A statement about the originality of work

Its non-submission/consideration in other journal. It is an original work no submitted in other journal.

Code availability

Not applicable.

Declaration of Competing Interest

The authors declare that they have no known competing financial interests or personal relationships that could have appeared to influence the work reported in this paper.

Availability of data and material

Available by specific demand to the corresponding author.

References

[1] E. Békássy-Molnár, Wine filtration by ceramic membranes, in: K. Bélafi-Bakó, L. Gubicza, M. Mulder (Eds.), Integration of Membrane Processes into Bioconversions, Springer, US, 2000, pp. 165–175.

[2] C. Peri, M. Riva, P. Decio, Crossflow membrane filtration of wines: comparison of performance of ultrafiltration, microfiltration, and intermediate cut-off membranes, Am. J. Enol. Vitic. 39 (2) (1988) 162–168. Jan. 1988.

[3] B. Hofs, J. Ogier, D. Vries, E.F. Beerendonk, E.R. Cornelissen, Comparison of ceramic and polymeric membrane permeability and fouling using surface water, Sep. Purif. Technol. 79 (3) (2011) 365–374, https://doi.org/10.1016/j.seppur.2011.03.025.

[4] S.W. King, R.J. Nemanich, R.F. Davis, Wet chemical processing of (0001)Si 6H-SiC. Hydrophobic and hydrophilic surfaces, J. Electrochem. Soc. 146 (5) (1999) 1910–1917, https://doi.org/10.1149/1.1391864.

[5] M.C. Fraga, S. Sanches, J.G. Crespo, V.J. Pereira, Assessment of a new silicon carbide tubular honeycomb membrane for treatment of olive mill wastewaters, Membranes 7 (2017) 1.

[6] L. Luo, X. Chen, Y. Wang, J. Yue, Z. Du, X. Huang, X.-Z. Tang, Bio-inspired modification of silicon carbide foams for oil/water separation and rapid power-free absorption towards highly viscous oils, Ceram. Int. 44 (11) (2018) 12021–12029, https://doi.org/10.1016/j.ceramint.2018.03.196.

[7] H. Sui, J. Dong, M. Wu, X. Li, R. Zhang, G. Wu, Continuous hydrogen production by dark fermentation in a foam SiC ceramic packed up-flow anaerobic sludge blanket reactor, Can. J. Chem. Eng. 95 (1) (2017) 62–68, https://doi.org/10.1002/cjce.22653.

[8] M. Zoubeik, A. Henni, Ultrafiltration of oil-in-water emulsion using a 0.04-μm silicon carbide membrane: Taguchi experimental design approach, Desalin. Water Treat. 62 (2016).

[9] T. Zsirai, H. Qiblawey, P. Buzatu, M. Al-Marri, S.J. Judd, Cleaning of ceramic membranes for produced water filtration, J. Pet. Sci. (2018).

[10] A.K. Bakshi, R. Ghimire, E. Sheridan, M. Kuhn, Treatment of produced water using silicon carbide membrane filters. Advances in Bioceramics and Porous Ceramics VIII, Wiley-Blackwell, 2015, pp. 89–106.

[11] C. He, Vidic, R.D, Application of microfiltration for the treatment of Marcellus Shale flowback water: Influence of floc breakage on membrane fouling, J. Membr. Sci. 510 (2016) (2016) 348–354, https://doi.org/10.1016/j.memsci.2016.03.023.

[12] M. Kuhn, A. Bakshi, E. Sheridan, F. Rodrigues, A. Vincent, M. Moeller, R. Neufert, Silicon carbide membranes for water filtration applications: ceramic transactions, Ceram. Environ. Syst. (2016) 119–128.

[13] M. Trevisan, L. Barthélémy, R. Ghidossi, P. Moulin, Silicon carbide (SiC) membranes in œnology: a laboratory-scale study, OENO One 54 (4) (2020) 719–732, https://doi.org/10.20870/oeno-one.2020.54.4.3856.

[14] V. Chen, H. Li, F. Ag, Non-invasive observation of synthetic membrane processes - a review of methods, J. Membr. Sci. 241 (1) (2004) 23–44, 2004.

[15] J. Vicente, Y. Wyart, P. Moulin, Characterization (two-dimensional;three-dimensional) of ceramic microfiltration membrane by synchrotron radiation: new and abraded membranes, J. Porous Media 16 (6) (2013) 2013, https://doi.org/10.1615/JPorMedia.v16.i6.50.

[16] N. Bossa, P. Chaurand, J. Vicente, D. Borschneck, C. Levard, O. Aguerre-Chariol, J. Rose, Micro- and nano-X-ray computed-tomography: a step forward in the characterization of the pore network of a leached cement paste, Cem. Concr. Res. 67 (2015) 138–147, https://doi.org/10.1016/j.cemconres.2014.08.007.

[17] Brun, E., Vicente, J., Topin, F. and Occelli, R. 2013. iMorph: A 3D morphological tool to fully analyze all kind of cellular materials. (2013), 6.

[18] Rootare, H.M. 1970. A Review of Mercury Porosimetry. Advanced Experimental Techniques in Powder Metallurgy: Based on a Symposium on Advanced Experimental Techniques in Powder Metallurgy sponsored by the Institute of Metals Division, Powder Metallurgy Committee, held at the Spring Meeting of The Metallurgical Society of AIME in Pittsburgh, Pennsylvania, May.

[19] A.W. Adamson, A.P. Gast, Physical Chemistry of Surfaces, Wiley, 1997.

[20] Tomographie à rayons X: 2013. ⟨https://www.techniques-ingenieur.fr/base-documentaire/mesures-analyses-th1/cnd-methodes-globales-et-volumiques-42585210/tomographie-a-rayons-x-p950/⟩. Accessed: 2020–10-13.

[21] Antoni Buades, A non-local algorithm for image denoising. Computer Vision and Pattern Recognition, 2005, pp. 60–65, https://doi.org/10.1109/CVPR.2005.38. CiteSeerX, ISBN 978-0-7695-2372-9.

[22] C.A. Schneider, W.S. Rasband, K.W. Eliceiri, NIH Image to ImageJ: 25 years of image analysis, Nat. Methods 9 (7) (2012) 671–675, https://doi.org/10.1038/nmeth.2089.

[23] M.L. González-Martín, L. Labajos-Broncano, B. Jańczuk, J.M. Bruque, Wettability and surface free energy of zirconia ceramics and their constituents, J. Mater. Sci. 34 (23) (1999) 5923–5926, https://doi.org/10.1023/A:1004767914895.

[24] S.-J. Lee, M. Dilaver, P.-K. Park, J.-H. Kim, Comparative analysis of fouling characteristics of ceramic and polymeric microfiltration membranes using filtration models, J. Membr. Sci. 432 (2013) 97–105, https://doi.org/10.1016/j.memsci.2013.01.013.

[25] E. Brun, C. Ferrero, J. Vicente, Fast granulometry operator for the 3D identification of cell structures, Fundam. Inform. (2017).

[26] J. Vicente, F. Topin, Open celled material structural properties measurement: from morphology to transport properties, Mater. Trans. (2006).

[27] Digabel,H., Lantuejoul, C., Iterative algorithms, (1977), Proc. of 2nd European Symposium or Quant. analysis of microstructures in material sciences, biology and medicine, Caen, France, 4–7 Oct,

[28] E.W. Dijkstra, A note on two problems in connexion with graphs, Numer. Math. 1 (1) (1959) 269–271, https://doi.org/10.1007/BF01386390.